Hidden symmetry-breaking in a kagome Ising ferromagnet

Tianxiong Han,^{1,2} Tyler J. Slade,¹ Liqin Ke,^{1,3} Qing-Ping Ding,¹ Minseong Lee,⁴ R. D. McKenzie,^{1,2} Bing Li,^{1,5} Dhurba R. Jaishi,^{1,2} Yongbin Lee,¹ D. M. Pajerowski,⁵ Qiang Zhang,⁵ Tao Hong,⁵ P. C. Canfield,^{1,2} Y. Furukawa,^{1,2} K. Thirunavukkuarasu,⁶ Aashish Sapkota,¹ Rebecca Flint,^{1,2} and R. J. McQueeney^{1,2}

¹Ames National Laboratory, U.S. DOE, Iowa State University, Ames, Iowa 50011, USA
²Department of Physics and Astronomy, Iowa State University, Ames, Iowa 50011, USA
³Department of Materials Science and Engineering, University of Virginia, Charlottesville, VA 22904
⁴National High Magnetic Field Laboratory, Los Alamos National Laboratory, Los Alamos, New Mexico 87545, USA
⁵Neutron Scattering Division, Oak Ridge National Laboratory, Oak Ridge, TN, 37831, USA
⁶Florida A&M University, Tallahassee, FL 32307 USA
(Dated: November 12, 2025)

Kagome metals can host unconventional electronic phenomena that emerge from their frustrated lattice geometry and associated band topology. Correlated electronic orders, such as charge-density waves and superconductivity, are observed to intertwine with subtle time-reversal symmetry breaking whose microscopic origin is not currently understood. Here, we provide evidence for such time-reversal symmetry breaking in the kagome metal TbV_6Sn_6 arising from staggered magnetic moments within the kagome layers. TbV_6Sn_6 consists of metallic V kagome layers separated by Tb triangular layers that host Ising ferromagnetic order. Deep in the ferromagnetic state, the Tb Ising doublet ground state should display a single, dispersionless spin-flip excitation. Instead, inelastic neutron scattering reveals two sharp excitations associated with inequivalent Tb sites, demonstrating that a symmetry-broken phase coexists with Ising ferromagnetism. No additional structural or magnetic phase transitions are detected, and first-principles calculations rule out lattice distortions as the origin of the splitting. We attribute this effect to time-reversal symmetry breaking encoded by small V moments that couple to the Tb sublattice and leave a measurable spectral fingerprint. Our results establish rare-earth local moment spectroscopy as a sensitive probe of subtle broken symmetries and highlight an unexpected interplay between kagome magnetism and rare-earth local moment magnetism.

Introduction. Kagome metals are widely studied for their capacity to host a variety of correlation-driven electronic states that arise from special features of their band structure [1–9]. Recently, there has been great interest in vanadiumbased AV_3Sb_5 kagome metals following the observation of charge-density wave (CDW) order [10–14]. This CDW state breaks translational symmetry and is also reported to simultaneously break time-reversal symmetry, presumably due to loop currents that form in concert with complex charge ordering [15, 16]. In this unique quantum state, the appearance of chiral superconductivity is a surprising development that provides a test bed to study the interrelationship between various correlation-driven symmetry-broken states [17, 18].

Beyond the AV₃Sb₅ family, other V-based kagome metals with distinct structural frameworks have also shown intriguing symmetry-breaking behavior. A CDW symmetrybreaking phase transition has recently been discovered in ScV₆Sn₆ from a different mechanism than that in the AV₃Sb₅ compounds [19, 20]. Muon spin resonance data suggest that time-reversal symmetry may also be broken in the CDW state [21]. Other RV₆Sn₆ compounds readily admit magnetic rareearth ions (R = Gd - Tm), allowing for the interplay of local moment magnetism with symmetry-broken metallic V kagome layers. Unfortunately, while the rare-earth moments in RV_6Sn_6 compounds order at low temperatures ($T_C < 5$ K) with transport anomalies highlighting the coupling to conduction electrons [22–26], no other symmetry-broken phases, such as CDW order, have been detected. However, the observation of large orbital magnetization in weak magnetic fields in TbV₆Sn₆ suggests that novel magnetic interplay with

kagome electrons is possible [27].

Here, we investigate the magnetic interactions in ${\rm TbV_6Sn_6}$ using inelastic neutron scattering (INS). ${\rm TbV_6Sn_6}$ is a ferromagnet (FM) [$T_{\rm C}=4.4$ K] with strong Ising anisotropy where Tb ions adopt a high-spin electronic doublet ground state [23, 24, 28]. In the FM state, this doublet is split by the molecular field of the surrounding Tb ions, and INS should detect a single spin-flip excitation between these two states. However, we observe two spin-flip excitations at different energies, rather than one, and conclude that symmetry-breaking is present which leads to two inequivalent Tb sites.

Due to the non-Kramers nature of the Tb ion (J=6), both crystallographic and time-reversal symmetry breaking can generate different crystalline-electric field (CEF) or molecular field magnitudes, respectively, that locally shift the spin-flip excitation energy. Our analysis of the spin-flip excitations and their temperature dependence indicates a presence of a staggered internal field that breaks translational and time-reversal symmetry well above $T_{\rm C}$. This hidden symmetry breaking is distinct from Tb ordering, with the most likely origin being small-moment antiferromagnetism that develops within the V kagome layers.

Magnetic Hamiltonian for TbV_6Sn_6 . The Tb ions in TbV_6Sn_6 have large angular momentum $(J=6, S=3, L=3, g_J=3/2)$ and are located on a triangular lattice with 6/mmm point group symmetry. The CEF Hamiltonian is $\mathcal{H}_{CEF}=B_2^0\mathcal{O}_2^0+B_4^0\mathcal{O}_4^0+B_6^0\mathcal{O}_6^0+B_6^6\mathcal{O}_6^6$, where B_l^m are CEF parameters and \mathcal{O}_l^m are Stevens operators [29]. The B_6^6 CEF parameter ultimately plays an important role, but in its absence all zero-field CEF states can be labeled by the az-

imuthal quantum number, $|J,m\rangle = |m\rangle$. Previous work [28] finds a $|m=\pm 6\rangle$ doublet ground state that is separated from the first excited state $|\pm 5\rangle$ by a large CEF energy of $\Delta \approx 8$ meV $\gg k_{\rm B}T_{\rm C}$, consistent with Ising character.

Tb moments **J** within the triangular layer are magnetically coupled through a combination of competing FM RKKY exchange and AFM dipolar couplings [22, 30]. As described in the SI, the effective nearest-neighbor coupling is $\mathcal{J} \approx \mathcal{J}_{RKKY} + \mathcal{J}_{dipolar}$ where $\mathcal{J}_{dipolar}/\mathcal{J}_{RKKY} \approx -0.20$. Single-crystal INS data find that the FM interlayer coupling \mathcal{J}_z is very weak and likely dipolar in origin, resulting in a quasi-2D Ising FM.

Expected excitation spectrum of an Ising FM. The strong uniaxial anisotropy of an Ising FM means that the magnetic moments can only point up or down. From the perspective of quantum states in TbV₆Sn₆, the up and down moments are represented by the $|\pm 6\rangle$ doublet ground state where the spin-flip transition from $|+6\rangle \rightarrow |-6\rangle$ is the characteristic excitation of an Ising FM. The spin-flip energy is the cost to flip one spin while all neighboring spins remain mutually parallel and is given by $\Delta_{SF} = z|\mathcal{J}|J\Delta m = 12|\mathcal{J}|J^2$ where z=6 is the coordination number for triangular lattice and $\Delta m=2J$, as shown in Fig. 1(a) and (b).

The spin-flip energy can be estimated from $T_{\rm C}$ by using the relation $k_{\rm B}T_{\rm C}=[4/\ln(3)]|\mathcal{J}|J^2$ for a 2D Ising FM [31]. We find that $\mathcal{J}\approx 2.9~\mu\text{eV}$ and $\Delta_{SF}\approx 1.3~\text{meV}$. Within a mean-field approximation, $\Delta_{SF}=2\beta J$ is caused by a molecular field of strength $\beta=z|\mathcal{J}|J\approx 0.10~\text{meV}$ [or $B_{\rm MF}=\beta/(g_J\mu_{\rm B})=1.2~\text{T}$]. Single-crystal INS data measuring the dispersion of the main CEF transition from $|+6\rangle \rightarrow |+5\rangle$ provide a consistent independent measure of \mathcal{J} (see SI).

Since only dipole-allowed transitions with $\Delta m=0,\pm 1$ are detectable with INS [32], the spin-flip transition with $\Delta m=12$ should not be observed. However, the spin-flip transition becomes weakly dipole-allowed when $B_6^6\mathcal{O}_6^6\propto J_\pm^6\neq 0$ since level mixing among $|\pm 6\rangle$ and $|0\rangle$ states opens a channel with $\Delta m=0$. As discussed below, a non-zero B_6^6 will also split the non-Kramers $|\pm 6\rangle$ Ising doublet by $\lesssim 0.01$ meV which is much smaller than the spin-flip energy.

Inelastic neutron scattering data. INS data reveal a different picture of the spin-flip excitations in TbV₆Sn₆ than that described above. We find two transitions (labeled E_1 and E_2) close to the estimated spin-flip energy of 1.3 meV, as shown in Fig. 1(c). At temperatures well below $T_{\rm C}$, Figs. 1(c) and (d) show that the excitations are sharp (resolution-limited), dispersionless, and have equal intensities. Given these traits and the proximity to the estimated Δ_{SF} , we identify both peaks as spin-flip excitations with a relative shift of $2\delta = E_2 - E_1 = 0.34$ meV.

When the temperature is increased, Figs. 2(a)-(c) show that 2δ is reduced and the Lorentzian full-width (Γ) broadens until $T_{\rm C}$ is reached. E_1 and E_2 have a component that is proportional to the FM order parameter below $T_{\rm C}$, but with opposite sign $(\pm\delta)$. Surprisingly, the spin-flip excitations do not vanish above $T_{\rm C}$, maintaining a constant energy shift of

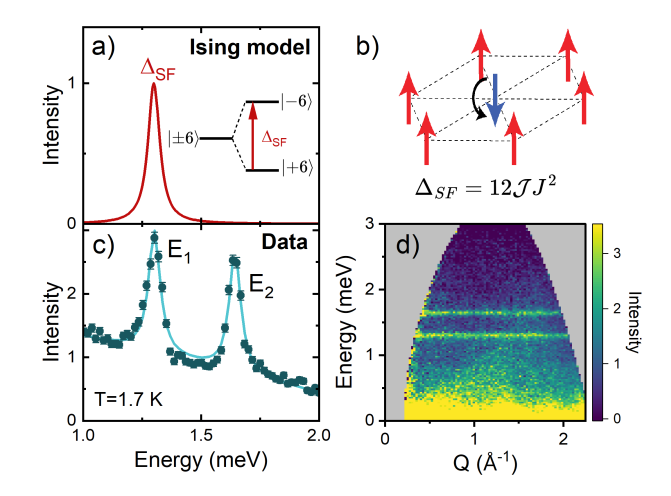


FIG. 1. Spin-flip excitations in an Ising ferromagnet. (a) Expected spin-flip excitation spectrum within the $|\pm 6\rangle$ doublet in the FM ordered state. The spectrum should consist of a single peak at $\Delta_{SF}\approx 1.3$ meV. (b) Schematic diagram of the spin-flip excitation. (c) Inelastic neutron scattering data from TbV₆Sn₆ at T=1.7 K showing two spin-flip excitations labeled E_1 and E_2 . (d) Full Q-E neutron spectrum of TbV₆Sn₆ at 1.7 K.

 $2\delta=0.16$ meV until at least 17.5 K. The average of E_1 and E_2 is temperature-independent and we identify it as the experimentally determined spin-flip energy $\Delta_{SF}=1.47$ meV (slightly larger than estimates from $T_{\rm C}$ noted above). Fig. 2(d) shows that the intensity of the two peaks weaken with increased temperature, but always maintain equal relative intensities.

Presumably, the persistence of spin-flip excitations above $T_{\rm C}$ is due to strong short-range FM correlations that are observed to persist up to at least 40 K (See SI Fig. S6). Unlike mean-field theory where the spin correlations and the molecular field vanish above $T_{\rm C}$, exact solutions of the Ising model show that robust nearest-neighbor spin correlations maintain a quantized value of the local field and corresponding spin-flip energy above $T_{\rm C}$ [33].

Thermal fluctuations will eventually suppress the spin-flip excitations at high enough temperature. Unfortunately, the spin-flip signals are overwhelmed above 20 K by the growth of other CEF excitations (see Ref. [28] for details). In this respect, we note that the spin-flip excitations are very weak, with intensities more than 400 times weaker than the main dipole-allowed $|+6\rangle \rightarrow |+5\rangle$ CEF transition out of the ground state. This weakness is expected due to the small dipole matrix element between the split doublet states, as noted above.

Analysis. We consider several possibilities to explain the presence of two spin-flip excitations in TbV_6Sn_6 . One possibility is that hyperfine interactions of the form AJ_zI_z lead to a splitting between coupled nuclear and electronic spin states. Terbium has a nuclear spin of I=3/2 and the estimated hyperfine coupling constant A=0.002 meV, as reported in Refs. [34, 35], is consistent with the nuclear Schottky anomaly observed in TbV_6Sn_6 [22]. Hyperfine coupling will result in four electronic spin dipole-allowed transitions, not two, and

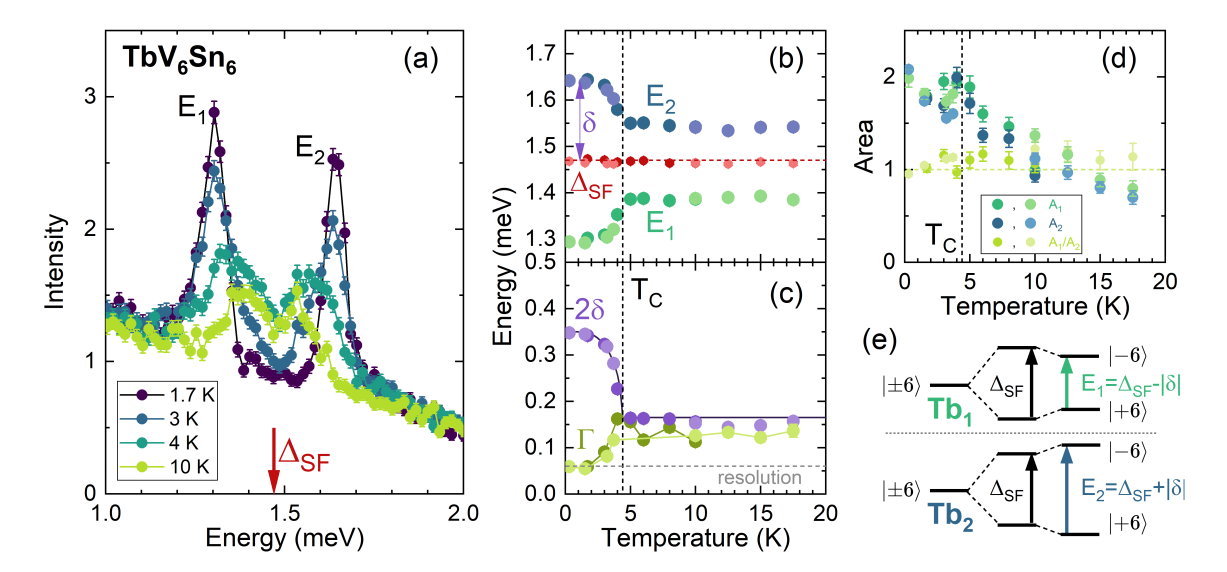


FIG. 2. Temperature evolution of spin-flip excitations in TbV₆Sn₆. (a) Inelastic neutron scattering data showing two spin-flip excitations at energies of E_1 and E_2 at temperatures above and below T_C . (b) Temperature dependence of E_1 and E_2 , average value (Δ_{SF}), and splitting parameter ($2\delta = E_2 - E_1$) as obtained from fitting INS spectra similar to panel (a). (c) Temperature dependence of 2δ and Lorentzian full-width Γ of the excitations. (d) The temperature dependence of the area of each peak along with the ratio of the areas A_1/A_2 . (e) Schematic level diagrams for two inequivalent Tb ions with different spin-flip energies caused by symmetry-breaking energy δ . In panels (b)-(d), different shading of symbols indicates independent measurements of different samples.

the overall splitting of $36A\approx 0.07$ meV is much smaller than 2δ and comparable to the instrumental resolution (0.06 meV full-width-at-half-maximum). Nuclear quadrupolar interactions are expected to be even smaller [36], and so we dismiss coupling to nuclear spins as a viable explanation.

The sharpness and equal intensity of the two peaks are more consistent with a scenario where a symmetry-breaking transition occurs which generates two inequivalent Tb sites (Tb₁ and Tb₂) with different CEFs or molecular exchange fields, as shown in Fig. 2(e). Given the subtle broken-symmetry phases found in other kagome metals, here we consider the possibility that either crystallographic or time-reversal symmetry is broken at temperatures well above $T_{\rm C}$, generating a symmetry-breaking field acting on the Tb ion with strength δ .

Crystallographic symmetry breaking. We first consider crystallographic symmetry breaking which can lead to siteto-site variation of the spin-flip energy due the non-Kramers' nature of the Tb ion. At high temperatures, all RV₆Sn₆ compounds adopt the P6/mmm space group with Tb located on the 1a Wyckoff site, i.e. all Tb sites are crystallographically equivalent. ScV₆Sn₆ is known to undergo a structural transition below 92 K that would generate inequivalent Sc sites [19, 20]. The CDW consists of trimerization of Sn-Sc-Sn units along the c-axis that are staggered in the plane. A distortion at $q_{CDW} = (1/3, 1/3, 1/3)$ creates two inequivalent Tb sites with multiplicity ratio of 2:1, which is inconsistent with the equal intensity of the spin-flip excitations. Various experimental studies have not detected a structural distortion in any RV_6Sn_6 compound other than R = Sc [22– 24, 37, 38]. Our temperature-dependent strain, single-crystal X-ray diffraction, powder neutron diffraction, nuclear magnetic resonance, and Raman scattering experiments (Fig. 3(d) and SI) find no evidence of CDW order or other structural transitions down to 2 K.

However, it is possible that subtle (not yet detected) crystallographic symmetry breaking is present or may occur close to $T_{\rm C}$ due to magnetoelastic interactions. ISODISTORT [39] predicts only one maximal subgroup which generates an equal population of unique Tb₁ and Tb₂ sites. This distortion with ${\bf q}=(0,0,1/2)$ is caused by the dimerization of Sn or V layers along c, as shown in Fig. 3(a). This generates local $\Delta c/c$ distortions with different B_6^6 values which leads to different ground state doublet splittings for Tb₁ and Tb₂.

In Fig. 3(b), calculations using point-charge models provided by PyCrystalField [40] and density-functional theory +U (DFT+U) predict changes in the B_l^m parameters when varying $\Delta c/c$. Fig. 3(c) shows that the spin-flip energies of the Tb₁ and Tb₂ sites are only slightly shifted ($\delta < 0.01 \text{ meV}$) by a large strain of $\Delta c/c=3\%$ (corresponding to a $\sim 30\%$ change in B_6^6), and δ is further suppressed by the molecular field. However, temperature-dependent strain measurements shown in the inset to Fig. 3(d) find a tiny spontaneous magnetostriction of $\Delta L/L < 0.003\%$ below $T_{\rm C}$. Upon warming up to 300 K, the lattice expands less than 0.5\% from both temperature-dependent strain and X-ray measurements. The differences between strain and X-ray results may come from the stacking of multiple pieces when measuring strain. X-ray diffraction data shown in Fig. 3(e) also find no evidence for (0,0,1/2)-type crystallographic symmetry lowering. While we cannot entirely dismiss crystallographic symmetry breaking as a source for δ for ions without Kramers degeneracy, we estimate that these effects are orders-of-magnitude too small to

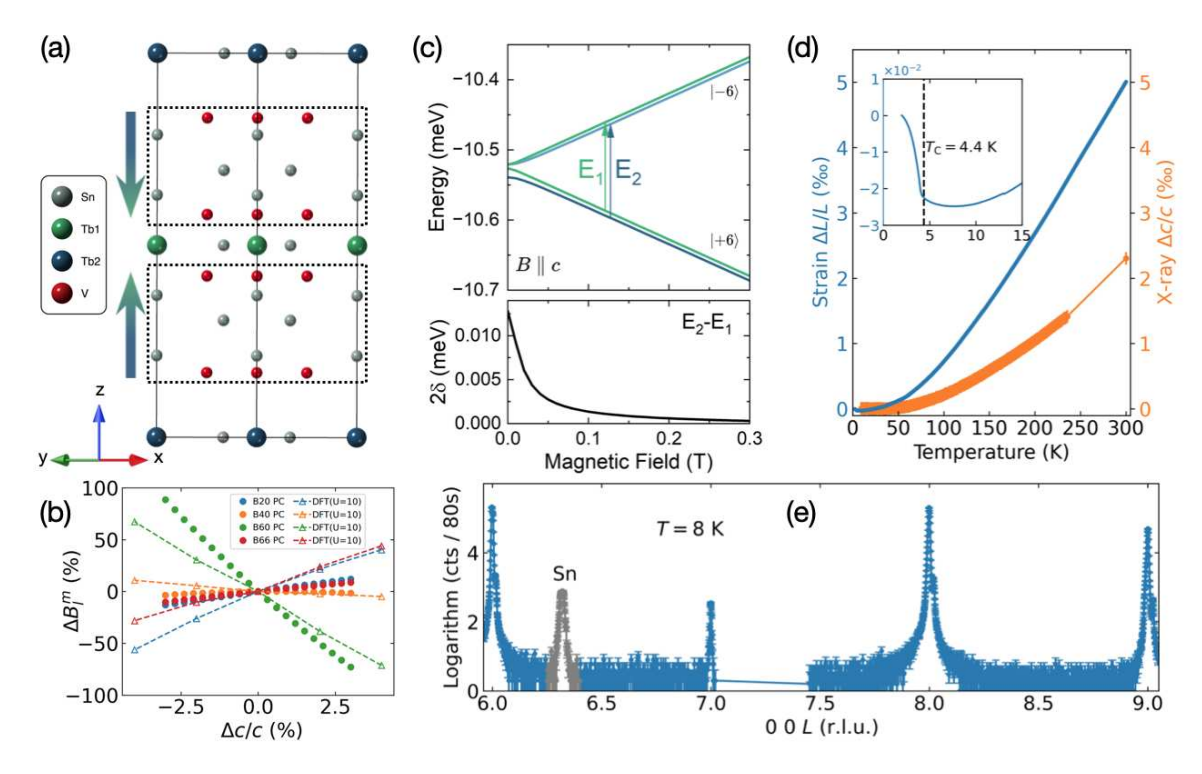


FIG. 3. Crystallographic-symmetry breaking. (a) A possible crystallographic-symmetry breaking scenario showing inequivalent Tb sites with equal multiplicities caused by (0,0,1/2) distortion. The displacement of the atoms in dashed boxes creates inequivalent Tb₁ (light blue atoms) and Tb₂ (dark blue) local environments with Tb-Sn layer distances $d_0 \pm \epsilon$ and can be understood as a local $\Delta c/c$ distortion. (b) The change of B_l^m parameters with $\Delta c/c$ lattice distortion using the point charge model (dots) and the DFT calculation (triangle with dashed lines) up to $\Delta c/c = 4\%$. (c) Evolution of the doublet splittings E_1 and E_2 in a molecular field along the c-axis in the presence of a large local distortion ($\Delta c/c = 3\%$) that generates Tb₁ and Tb₂ ions with B_6^6 values shifted $\pm 30\%$. The lower panel shows that the zero-field shift $2\delta < 0.015$ meV is suppressed by the molecular field. (d) Temperature-dependent strain ($\Delta L/L$) and X-ray diffraction measurements ($\Delta c/c$). The inset shows a spontaneous magnetostriction of $\Delta L/L \sim 0.002\%$ is observed below T_C . (e) Logarithm of XRD intensity along (0 0 L) direction at 8 K. No half-integer L peaks are observed that correspond to $\mathbf{q} = (0,0,1/2)$ symmetry breaking. The Bragg peak corresponding to the Sn impurity is colored in gray. The shoulders next to the Bragg peaks are from Cu-K α_2 incident X-ray.

account for the observed splitting shown in Fig. 2.

Time-reversal symmetry breaking. We now consider the possibility that an interaction exists with the Tb sublattice which breaks time-reversal symmetry. Here, we speak of time-reversal symmetry breaking that is distinct from FM ordering of the Tb ions and presumably arises from the V layers. To deliver two different spin-flip energies, this must take the form of a staggered field that also breaks translational symmetry (i.e. antiferromagnetic) as shown in Fig. 4.

However, no such staggered magnetism has been directly detected by neutron diffraction. We investigated potential V magnetism using ^{51}V nuclear magnetic resonance (NMR) measurements on single-crystal and polycrystalline samples of TbV6Sn6 performed at a Larmor field of 7 T, as described in the SI. In the FM ordered phase, the NMR resonance shifts away from the Larmor field by 0.39 T, but no splitting is observed that would indicate AFM order. By accounting for several contributions to the shift, including macroscopic and dipolar fields, we cannot rule out the existence of a small V moment $\sim 0.02~\mu_B$. This suggests tiny itinerant V moments may exist, perhaps originating from orbital magnetization similar to that reported in Ref. [27].

We hypothesize that an intersublattice magnetic coupling exists of the form $\mathcal{J}^{TV}\mathbf{J}\cdot\mathbf{s}$ that couples the Tb moment (J) to a staggered spin degree-of-freedom associated with the V layers (s). To account for the splitting observed above T_{C} , the V AFM order must set in above T_{C} with some unknown exchange energy scale, $T_N\sim\mathcal{J}^{VV}s^2$. The V magnetic configuration cannot be directly determined from INS data, but we discuss some possibilities below.

In Fig. 4(a), we show two unique Tb sites that appear between stripe-like AFM V layers with FM V-V interlayer coupling. Tb2 resides in a V generated field of $\delta=12Js\mathcal{J}^{TV}$ and Tb1 in a field of $-\delta$. The INS data provide an estimate of $s\mathcal{J}^{TV}\approx 0.002$ meV which is significantly smaller than that found in ferrimagnetic TbMn6Sn6 ($s\mathcal{J}^{TM}=1.8$ meV) with large Mn moments [41]. A key constraint for this scenario is that the Tb sublattice must remain FM in the presence of AFM V order. Therefore, there must be an energy barrier that prevents the Tb1 site from flipping parallel to the V moments. This condition $\Delta_{SF}>3\delta/2$ is easily satisfied and guarantees that two spin-flip excitations will be observed.

Fig. 4(b) shows a scenario where FM V layers are staggered in an up-up-down-down configuration with q = (0, 0, 1/2),

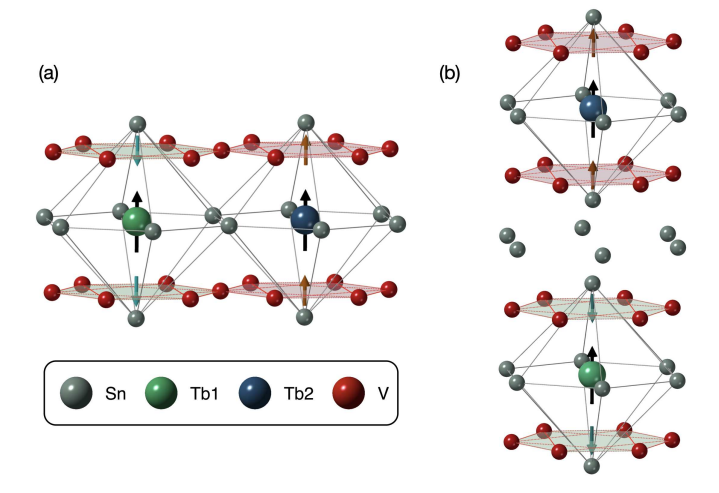


FIG. 4. **Time-reversal symmetry breaking.** Different magnetic environments of Tb₁ and Tb₂ ions due to (a) stripe-like antiferromagnetic order within the V kagome layer and (b) up-up-down-down AFM stacking of FM V layers.

leading to inequivalent Tb₁ and Tb₂ sites in a similar fashion to the crystallographic distortion shown in Fig. 3(a). In this scenario, FM order on the Tb sublattice must be maintained by Tb-Tb interlayer coupling (\mathcal{J}_z) such that $\mathcal{J}_zJ^2 > \delta/2$, but the dispersionless character of the main CEF excitation perpendicular to the layer provides an upper limit of $\mathcal{J}_z < 0.0015$ meV. Thus, the scenario in Fig. 4(b) appears unfeasible as it interactions will favor AFM Tb order.

The temperature dependence of $\delta(T)$ shown in Fig. 2(c) can naturally be explained if the Tb and V order parameters have an attractive quadratic Landau coupling, $-\gamma M_{Tb}^2 N_V^2$, where N_V is the V staggered magnetization. This coupling would cause a change in the proposed V order parameter just below $T_{\rm C}$, $\Delta N_V(T) \propto M_{Tb}(T)^2$ that shifts the two spin-flip excitation energies in opposite directions. The fit of $\delta(T)$ versus the (1 0 0) Bragg peak intensities, shown in the SI, agrees with $\delta(T) \propto M_{
m Th}^2$ near the transition. By contrast, $\delta(T) \propto M_{
m Tb}$ would imply a ferromagnetic V order M_V , with a linear coupling, $\gamma M_{Tb} M_V$. This scenario cannot explain the two distinct Tb sites whose spin-flip excitations move in opposite directions below $T_{\rm C}$, and the $\gamma = 0$ phase transition $T_{\rm C}$ would be smeared out by the effective field due to M_V to a degree that is inconsistent with the specific heat data [24]. Therefore, a stripe-like antiferromagnetic V ordering is the most consistent with our data.

 $\it Discussion.$ In $\it TbV_6Sn_6$, the strong Ising character of the ground state limits the possible magnetic excitations that can occur in the FM ordered phase. We have, in essence, the simplest possible quantum system consisting of a doublet that is split by its local environment. This will result in a single spin-flip excitation when all Tb sites are equivalent. The observation of two spin-flip excitations can only arise when two inequivalent Tb ions reside in different local environments. The relative shift in the doublet splittings therefore acts as a very sensitive probe of the local symmetry-breaking and its

strength.

Our analysis shows that the doublet splitting of Tb_1 or Tb_2 is dominated by the exchange field of the surrounding Tb ions (Δ_{SF}) combined with a weaker symmetry-breaking interaction $\delta/\Delta_{SF}\approx 10\%$. Due to the non-Kramers nature of the Tb ion, this interaction can arise from either crystallographic or time-reversal symmetry breaking, although we argue that any crystallographic symmetry-breaking contributes $\ll 1\%$ to the local field. Thus, it is much more likely that Tb ions experience a staggered internal field that breaks both time-reversal and translational symmetries.

Outside of Tb itself, the origin of time-reversal symmetry breaking could only arise from spins or orbital motion of electrons within the V kagome layers. We hypothesize that magnetic V-V interactions drive AFM order that sets in well above $T_C = 4.4$ K, but V carries a small moment that so far has not been detected by neutron diffraction, but cannot be ruled out by NMR data. For local V spins, the development of robust AFM order within a kagome layer [Fig. 4(a)] may be hampered by geometric frustration. Another possibility is the development of orbital magnetization within the kagome layers. It has been shown that weak external magnetic fields can strongly split Dirac cones near E_F , resulting in spin Berry curvature that generates a momentum-dependent orbital magnetization which is peaked near the K-point in the Brillouin zone [27]. However, it is not clear whether such orbital moments can spontaneously form and order.

In any case, the proposed coupling between V and Tb moments is small, with V providing an effective staggered magnetic field of 0.15 T acting on the Tb site. This is $\sim\!1000$ times weaker than the Mn molecular field experienced by Tb in ferrimagnetic TbMn₆Sn₆ [42–44]. Other methods, such as muon spectroscopy, should be employed to provide additional evidence for potentially novel magnetism occurring within the kagome bands.

Summary. We report the observation of two spin-flip excitations in the Ising FM ${\rm TbV_6Sn_6}$ that originate from distinct Tb local environments. We hypothesize that the local environments are distinguished by small, staggered magnetic moments occurring on the V kagome sublattice. Although the V magnetic order has not been directly detected, it nevertheless breaks translational symmetry at the rare-earth sites and give rise staggered molecular field and a measurable splitting in the rare-earth spin excitation spectrum. These findings indicate a novel time-reversal symmetry breaking in the kagome electrons and establish a new method for detecting subtle symmetry breaking in quantum materials.

METHODS

Crystal growth and characterization. Single crystals of TbV_6Sn_6 were synthesized using the Sn flux method. Highpurity elemental Tb (Ames Lab, 99.99%), V (Alpha-Aesar, 99.99%), and Sn (Alpha-Aesar, 99.99%) were combined in a molar ratio of 1:6:60 and placed into the growth chamber

of a 5 ml alumina Canfield crucible set [45]. The crucibles were sealed under vacuum in a fused silica ampule and heated in a box furnace to 1180 °C. After holding at 1180 °C for \approx 24 h, the samples were removed from the furnace and the liquid decanted in a metal centrifuge, upon which the liquid phase is cleanly captured in the second crucible on the top side of the crucible set. This first step allows us to cleanly separate the liquid from any undissolved V [46]. A second sequence is then carried out, with the captured decant used in the "growth" side of a new crucible set. The second crucible set was sealed under vacuum as before and warmed in a box furnace to 1195 °C. After holding at 1195 °C for 6 h, the furnace was cooled to $775\,^{\circ}\mathrm{C}$ over $\sim 200\,\mathrm{h}$, upon which the ampule was removed from the furnace and the excess liquid decanted. Once cool, the ampules and crucibles were opened to reveal relatively large (10-30 mg), single-phase, crystals of TbV₆Sn₆. The polycrystalline sample was prepared by grinding the single crystal using a mortar and pestle, and sieving with a diameter of 32 micrometers to obtain particles of uniform size.

Inelastic neutron scattering measurements. INS measurements on polycrystalline and single-crystal samples of TbV₆Sn₆ were performed on the Cold Neutron Chopper Spectrometer (CNCS) at the Spallation Neutron Source at Oak Ridge National Laboratory using incident neutron energies of $E_i=3.32$ meV and 12 meV. The measured INS intensity is proportional to the spin-spin correlation function $\mathcal{S}(Q,\omega)$ with Q being the momentum transfer, and $\omega=\Delta E/\hbar$ being the energy transfer. The data is histogrammed with bin sizes of $\delta E=0.06$ meV and $\delta Q=0.02$ Å $^{-1}$ using DAVE software [47]. After integrating the intensity over the range $0.1 \leq Q \leq 2.7$, the resulting spectrum is fit using a Lorentzian function, accounting for both the instrumental and intrinsic resolutions through convolution.

Neutron Diffraction. We performed neutron powder diffraction measurements using the time-of-flight powder diffractometer POWGEN at Spallation Neutron Source at Oak Ridge National Laboratory. Approximately 1.3 grams of samples were prepared after grinding single crystals to a fine powder and sieved with 32 $\mu \rm m$. Diffraction patterns were collected in the paramagnetic regime at 15 K and the FM ordered state at 1.5 K using a neutron beam with a center wavelength of 2.665 Å. Rietveld refinements using the FullProf suite [48] were performed to determine the magnetic structure.

Neutron diffraction measurements were also performed on the powder sample of TbV_6Sn_6 using the cold neutron triple-axis spectrometer (CTAX) at High Flux Isotope Reactor (HFIR), ORNL, to get the order parameter. PG(002) monochromators and analyzers were used. Both the incident and final neutron energies were set to 3.5 meV. A cooled Be filter was placed after the sample table to remove the higher-order harmonics.

X-ray diffraction. High-resolution single-crystal X-ray diffraction measurements were performed at Ames National Laboratory using a four-circle diffractometer with $Cu-K\alpha_1$ radiation from a rotating-anode source and a Ge (1, 1, 1)

monochromator. The sample was attached to a flat Cu mount which was thermally anchored to the cold head of a He closed-cycle refrigerator. Be domes were used as vacuum shrouds and heat shields. A small amount of He exchange gas facilitated thermal equilibrium. The lattice constant c was measured with $\theta-2\theta$ scans at $\mathbf{Q}=(0,0,8)$ while warming from 8 K to 300K. Measurement along (0,0,L) direction is performed at 8 K.

Temperature-dependent strain. The temperature-dependent strain was measured using the dilatometry option of the Quantum Design DynaCool system. The measurement principle and setup are described in detail by Martien et. al. [49]. To enhance measurement sensitivity, five single crystals were stacked along the crystallographic c-axis. Since the total thickness was insufficient to fill the dilatometer gap, a FuSi spacer provided by Quantum Design was added to fill the remaining space; no adhesive was used in the assembly. The thermal dilation of the FuSi spacer was measured independently, and the final sample signal was obtained by subtracting the FuSi background from the combined FuSi-plus-sample measurement.

Nuclear magnetic resonance. The nuclear magnetic resonance (NMR) measurements of $^{51}{\rm V}$ nuclei ($I=\frac{7}{2},\frac{\gamma_{\rm N}}{2\pi}=$ 11.193 MHz/T, Q = -0.052 barns) were conducted on single crystals and a loosely packed powder using a laboratorybuilt phase-coherent spin-echo pulse spectrometer by sweeping the magnetic field B at fixed resonance frequencies f =78.35 MHz and f = 75.50 MHz. For the NMR measurements on the plate-like shaped TbV₆Sn₆ single crystals, multiple crystals were used with c-direction aligned. Field was applied either parallel or perpendicular to the crystaliline caxis. A loosely packed powder sample crushed from the single crystals was also used for comparison, in which the large FM anisotropic c-axis would align under a strong magnetic field. NMR measurements are performed at multiple temperatures below T=10 K. Above 10 K, the nuclear spin-spin relaxation rate $1/T_2$ increases rapidly, leading to a strong reduction of the NMR signals, making the measurements difficult.

DFT+U calculations. Crystal-field (CEF) parameters are calculated as a function of the aspect ratio $\frac{c}{a}$ while keeping the experimentally adopted volume constant. At each $\frac{c}{a}$ value, the CEF parameters are obtained using the total energy mapping method within the constrained DFT+U framework [28, 50]. The magnetocrystalline anisotropy energy profiles $E(\theta, \phi)$ are determined from total energy calculations as a function of the spin quantization direction. It is essential to enforce convergence at each spin orientation to the designated 4f state within this procedure [51]. The validity of this total energy mapping method rests on two recent demonstrations of the success of DFT-based approaches to rare-earth magnetism. First, excellent agreement between experimental and theoretical 4f anisotropy has been achieved across dozens of rare-earth-containing compounds, provided the Hund's rule ground state is enforced [7, 23, 28, 42, 51–53]. Second, the combination of DFT with crystal field theory has recently been validated [50]; in the present work, we also confirmed

that the extracted CEF parameters can perfectly reproduce the $E(\theta,\phi)$ profiles across all $\frac{c}{a}$ values.

Self-consistent DFT+U calculations, including spin-orbit coupling (SOC), were performed to evaluate the total energy $E(\theta,\phi)$ as a function of spin quantization directions, characterized by the polar and azimuthal angles θ and ϕ , using the full-potential linearized augmented plane wave (FP-LAPW) method as implemented in WIEN2K [54]. A large value of U=10 eV was employed to push the 4f states further below the Fermi level [55], and spin-orbit coupling was included using the second-variation approach [56, 57]. At each spin direction, we ensured that the constrained DFT+U calculations converged to the Hund's rule ground state of Tb³⁺, consistent with experimental results, thereby avoiding the otherwise unphysical DFT+U ground states that arise primarily from the orbital dependence of self-interaction errors [51]. Further details of the constrained DFT+U calculations of MAE can be found in Ref. [51].

ACKNOWLEDGMENTS

Inelastic neutron scattering data analysis (T.H., D.J., R.J.M.), X-ray diffraction (A.S.), nuclear magnetic resonance measurements (Q.-P.D., Y.F.), analytical theory (R.D.M., R.F.), and density-functional theory (Y.L., L.K.) calculations performed at the Ames National Laboratory are supported by the U.S. Department of Energy, Office of Science, Basic Energy Sciences, Materials Science and Engineering. Preparation of sample specimens and their characterization (T.J.S., P.C.) is supported by the Center for the Advancement of Topological Semimetals (CATS), an Energy Frontier Research Center funded by the U.S. Department of Energy (DOE) Office of Science (SC), Office of Basic Energy Sciences (BES), through the Ames National Laboratory. Ames National Laboratory is operated for the USDOE by Iowa State University under Contract No. DE-AC02-07CH11358. This research used resources at the Spallation Neutron Source and High Flux Isotope Reactor, DOE Office of Science User Facilities operated by the Oak Ridge National Laboratory. The neutron beam time was allocated to CNCS on proposal number IPTS-29896 and IPTS-33326, POWGEN on proposal number IPTS-31418, and CTAX on proposal number IPTS-32293. Dilatometry measurements (M.L.) acknowledge support from the LDRD program at Los Alamos National Laboratory. A portion of this work was performed at the National High Magnetic Field Laboratory, which is supported by the National Science Foundation Cooperative Agreement No. DMR-2128556* and the State of Florida and the U.S. Department of Energy.

- L. Kautzsch, S. S. Zhang, G. Chang, I. Belopolski, Q. Zhang, T. A. Cochran, D. Multer, M. Litskevich, Z.-J. Cheng, X. P. Yang, Z. Wang, R. Thomale, T. Neupert, S. D. Wilson, and M. Z. Hasan, Unconventional chiral charge order in kagome superconductor KV₃Sb₅, Nat. Mater. **20**, 1353 (2021).
- [2] X. Teng, L. Chen, F. Ye, E. Rosenberg, Z. Liu, J.-X. Yin, Y.-X. Jiang, J. S. Oh, M. Z. Hasan, K. J. Neubauer, B. Gao, Y. Xie, M. Hashimoto, D. Lu, C. Jozwiak, A. Bostwick, E. Rotenberg, R. J. Birgeneau, J.-H. Chu, M. Yi, and P. Dai, Discovery of charge density wave in a kagome lattice antiferromagnet, Nature 609, 490 (2022).
- [3] H. Tan, Y. Liu, Z. Wang, and B. Yan, Charge density waves and electronic properties of superconducting kagome metals, Phys. Rev. Lett. 127, 046401 (2021).
- [4] B. R. Ortiz, P. M. Sarte, E. M. Kenney, M. J. Graf, S. M. L. Teicher, R. Seshadri, and S. D. Wilson, Superconductivity in the \mathbb{Z}_2 kagome metal KV₃Sb₅, Phys. Rev. Mater. **5**, 034801 (2021).
- [5] B. R. Ortiz, L. C. Gomes, J. R. Morey, M. Winiarski, M. Bordelon, J. S. Mangum, I. W. H. Oswald, J. A. Rodriguez-Rivera, J. R. Neilson, S. D. Wilson, E. Ertekin, T. M. McQueen, and E. S. Toberer, New kagome prototype materials: discovery of KV₃Sb₅,RbV₃Sb₅, and CsV₃Sb₅, Phys. Rev. Mater. 3, 094407 (2019).
- [6] Y.-F. Zhang, X.-S. Ni, T. Datta, M. Wang, D.-X. Yao, and K. Cao, Ab initio study of spin fluctuations in the itinerant kagome magnet FeSn, Phys. Rev. B 106, 184422 (2022).
- [7] Y. Lee, R. Skomski, X. Wang, P. P. Orth, Y. Ren, B. Kang, A. K. Pathak, A. Kutepov, B. N. Harmon, R. J. McQueeney, I. I. Mazin, and L. Ke, Interplay between magnetism and band topology in the kagome magnets RMn₆Sn₆, Phys. Rev. B 108, 045132 (2023).
- [8] J.-X. Yin, W. Ma, T. A. Cochran, X. Xu, S. S. Zhang, H.-J. Tien, N. Shumiya, G. Cheng, K. Jiang, B. Lian, Z. Song, G. Chang, I. Belopolski, D. Multer, M. Litskevich, Z.-J. Cheng, X. P. Yang, B. Swidler, H. Zhou, H. Lin, T. Neupert, Z. Wang, N. Yao, T.-R. Chang, S. Jia, and M. Zahid Hasan, Quantum-limit Chern topological magnetism in TbMn₆Sn₆, Nature 583, 533 (2020).
- [9] S. Baidya, S. Kang, C. H. Kim, and J. Yu, Chern insulator with a nearly flat band in the metal-organic-framework-based Kagome lattice, Sci. Rep. 9, 13807 (2019).
- [10] Z. Liang, X. Hou, F. Zhang, W. Ma, P. Wu, Z. Zhang, F. Yu, J.-J. Ying, K. Jiang, L. Shan, Z. Wang, and X.-H. Chen, Three-dimensional charge density wave and surface-dependent vortex-core states in a kagome superconductor CsV₃Sb₅, Phys. Rev. X 11, 031026 (2021).
- [11] K. Y. Chen, N. N. Wang, Q. W. Yin, Y. H. Gu, K. Jiang, Z. J. Tu, C. S. Gong, Y. Uwatoko, J. P. Sun, H. C. Lei, J. P. Hu, and J.-G. Cheng, Double superconducting dome and triple enhancement of T_c in the kagome superconductor $\mathrm{CsV_3Sb_5}$ under high pressure, Phys. Rev. Lett. **126**, 247001 (2021).
- [12] F. Du, S. Luo, B. R. Ortiz, Y. Chen, W. Duan, D. Zhang, X. Lu, S. D. Wilson, Y. Song, and H. Yuan, Pressure-induced double superconducting domes and charge instability in the kagome metal KV₃Sb₅, Phys. Rev. B 103, L220504 (2021).
- [13] H. Li, T. T. Zhang, T. Yilmaz, Y. Y. Pai, C. E. Marvinney, A. Said, Q. W. Yin, C. S. Gong, Z. J. Tu, E. Vescovo, C. S. Nelson, R. G. Moore, S. Murakami, H. C. Lei, H. N. Lee, B. J. Lawrie, and H. Miao, Observation of unconventional charge density wave without acoustic phonon anomaly in kagome superconductors AV_3Sb_5 (A=Rb, Cs), Phys. Rev. X 11, 031050 (2021).
- [14] J. Graham, C. Mielke III, D. Das, T. Morresi, V. Sazgari,

^[1] Y.-X. Jiang, J.-X. Yin, M. M. Denner, N. Shumiya, B. R. Ortiz, G. Xu, Z. Guguchia, J. He, M. S. Hossain, X. Liu, J. Ruff,

- A. Suter, T. Prokscha, H. Deng, R. Khasanov, S. Wilson, *et al.*, Depth-dependent study of time-reversal symmetry-breaking in the kagome superconductor AV_3Sb_5 , Nature Communications **15**, 8978 (2024).
- [15] M. M. Denner, R. Thomale, and T. Neupert, Analysis of Charge Order in the Kagome Metal AV_3Sb_5 (A = K, Rb, Cs), Phys. Rev. Lett. **127**, 217601 (2021).
- [16] C. Mielke III, D. Das, J.-X. Yin, H. Liu, R. Gupta, Y.-X. Jiang, M. Medarde, X. Wu, H. C. Lei, J. Chang, *et al.*, Time-reversal symmetry-breaking charge order in a kagome superconductor, Nature **602**, 245 (2022).
- [17] X. Feng, K. Jiang, Z. Wang, and J. Hu, Chiral flux phase in the kagome superconductor AV₃Sb₅, Science Bulletin 66, 1384 (2021).
- [18] S.-L. Yu and J.-X. Li, Chiral superconducting phase and chiral spin-density-wave phase in a hubbard model on the kagome lattice, Phys. Rev. B 85, 144402 (2012).
- [19] H. W. S. Arachchige, W. R. Meier, M. Marshall, T. Matsuoka, R. Xue, M. A. McGuire, R. P. Hermann, H. Cao, and D. Mandrus, Charge density wave in kagome lattice intermetallic ScV₆Sn₆, Phys. Rev. Lett. 129, 216402 (2022).
- [20] S. Lee, C. Won, J. Kim, J. Yoo, S. Park, J. Denlinger, C. Jozwiak, A. Bostwick, E. Rotenberg, R. Comin, *et al.*, Nature of charge density wave in kagome metal ScV₆Sn₆, npj Quantum Materials 9, 15 (2024).
- [21] Z. Guguchia, D. Gawryluk, S. Shin, Z. Hao, C. Mielke Iii, D. Das, I. Plokhikh, L. Liborio, J. K. Shenton, Y. Hu, *et al.*, Hidden magnetism uncovered in a charge ordered bilayer kagome material ScV₆Sn₆, Nature communications 14, 7796 (2023).
- [22] Y. Zhou, M.-K. Lee, S. Hammouda, S. Devi, S.-I. Yano, R. Sibille, O. Zaharko, W. Schmidt, K. Schmalzl, K. Beauvois, E. Ressouche, P.-C. Chang, C.-H. Huang, L.-J. Chang, T. Brückel, and Y. Su, Ground-state magnetic structures of topological kagome metals $RV_6\mathrm{Sn}_6$ ($R=\mathrm{Tb},\mathrm{Dy},\mathrm{Ho},\mathrm{Er}$), Phys. Rev. Res. **6**, 043291 (2024).
- [23] E. Rosenberg, J. M. DeStefano, Y. Guo, J. S. Oh, M. Hashimoto, D. Lu, R. J. Birgeneau, Y. Lee, L. Ke, M. Yi, and J.-H. Chu, Uniaxial ferromagnetism in the kagome metal ${\rm TbV_6Sn_6}$, Phys. Rev. B **106**, 115139 (2022).
- [24] G. Pokharel, B. Ortiz, J. Chamorro, P. Sarte, L. Kautzsch, G. Wu, J. Ruff, and S. D. Wilson, Highly anisotropic magnetism in the vanadium-based kagome metal ${\rm TbV_6Sn_6}$, Phys. Rev. Mater. **6**, 104202 (2022).
- [25] X.-Y. Zeng, H. Wang, X.-Y. Wang, J.-F. Lin, J. Gong, X.-P. Ma, K. Han, Y.-T. Wang, Z.-Y. Dai, and T.-L. Xia, Magnetic and magnetotransport properties in the vanadium-based kagome metals $\mathrm{DyV}_6\mathrm{Sn}_6$ and $\mathrm{HoV}_6\mathrm{Sn}_6$, Phys. Rev. B 109, 104412 (2024).
- [26] X. Zhang, Z. Liu, Q. Cui, Q. Guo, N. Wang, L. Shi, H. Zhang, W. Wang, X. Dong, J. Sun, Z. Dun, and J. Cheng, Electronic and magnetic properties of intermetallic kagome magnets $RV_6\mathrm{Sn}_6(R=\mathrm{Tb-Tm})$, Phys. Rev. Mater. **6**, 105001 (2022).
- [27] H. Li, S. Cheng, G. Pokharel, P. Eck, C. Bigi, F. Mazzola, G. Sangiovanni, S. D. Wilson, D. Di Sante, Z. Wang, *et al.*, Spin berry curvature-enhanced orbital zeeman effect in a kagome metal, Nature Physics 20, 1103 (2024).
- [28] T. Han, R. D. McKenzie, J. Blawat, T. J. Slade, Y. Lee, D. M. Pajerowski, J. Singleton, B. Li, P. C. Canfield, L. Ke, R. McDonald, R. Flint, and R. J. McQueeney, Proximity to quantum criticality in the ising ferromagnet TbV₆Sn₆ (2024), arXiv:2412.02010 [cond-mat.str-el].
- [29] E. Bauer and M. Rotter, Magnetism of complex metallic alloys: Crystalline electric field effects, in *Properties and Applications of Complex Intermetallics*, pp. 183–248.

- [30] Z. Porter, G. Pokharel, J.-W. Kim, P. J. Ryan, and S. D. Wilson, Incommensurate magnetic order in the F_2 kagome metal GdV_6Sn_6 , Phys. Rev. B **108**, 035134 (2023).
- [31] G. F. Newell, Crystal statistics of a two-dimensional triangular ising lattice, Physical Review 79, 876 (1950).
- [32] A. T. Boothroyd, Principles of Neutron Scattering from Condensed Matter (Oxford University Press, 2020).
- [33] M. Thomsen, M. F. Thorpe, T. C. Choy, and D. Sherrington, Local magnetic field distributions: Two-dimensional ising models, Phys. Rev. B 30, 250 (1984).
- [34] B. Bleaney and R. W. Hill, Hyperfine structure in terbium metal, Proceedings of the Physical Society 78, 313 (1961).
- [35] J. M. Baker and B. Bleaney, The nuclear spin and magnetic moment of terbium 159, Proceedings of the Physical Society. Section A 68, 257 (1955).
- [36] J. Kötzler and G. Raffius, Effect of quadrupolar interactions on the magnetic transitions of the terbium-monopnictides, Zeitschrift für Physik B Condensed Matter 38, 139 (1980).
- [37] G. Pokharel, S. M. L. Teicher, B. R. Ortiz, P. M. Sarte, G. Wu, S. Peng, J. He, R. Seshadri, and S. D. Wilson, Electronic properties of the topological kagome metals YV₆Sn₆ and GdV₆Sn₆, Phys. Rev. B 104, 235139 (2021).
- [38] H. Ishikawa, T. Yajima, M. Kawamura, H. Mitamura, and K. Kindo, GdV_6Sn_6 : a multi-carrier metal with non-magnetic 3 d-electron kagome bands and 4 f-electron magnetism, Journal of the Physical Society of Japan **90**, 124704 (2021).
- [39] B. J. Campbell, H. T. Stokes, D. E. Tanner, and D. M. Hatch, Isodisplace: a web-based tool for exploring structural distortions, Applied Crystallography 39, 607 (2006).
- [40] A. Scheie, PyCrystalField: software for calculation, analysis and fitting of crystal electric field Hamiltonians, Journal of Applied Crystallography 54, 356 (2021).
- [41] S. Riberolles, T. J. Slade, R. Dally, P. Sarte, B. Li, T. Han, H. Lane, C. Stock, H. Bhandari, N. Ghimire, *et al.*, Orbital character of the spin-reorientation transition in TbMn₆Sn₆, Nature Communications 14, 2658 (2023).
- [42] S. X. M. Riberolles, T. J. Slade, D. L. Abernathy, G. E. Granroth, B. Li, Y. Lee, P. C. Canfield, B. G. Ueland, L. Ke, and R. J. McQueeney, Low-temperature competing magnetic energy scales in the topological ferrimagnet TbMn₆Sn₆, Phys. Rev. X 12, 021043 (2022).
- [43] S. Riberolles, T. J. Slade, T. Han, B. Li, D. Abernathy, P. Can-field, B. Ueland, P. Orth, L. Ke, and R. McQueeney, Chiral and flat-band magnetic quasiparticles in ferromagnetic and metallic kagome layers, Nature Communications 15, 1592 (2024).
- [44] N. L, T. Victa Trevisan, and R. J. McQueeney, High-field magnetic phase diagrams of the $R\mathrm{Mn_6Sn_6}$ ($R=\mathrm{Gd}--\mathrm{Tm}$) kagome metals, Phys. Rev. B **111**, 054410 (2025).
- [45] P. C. Canfield, T. Kong, U. S. Kaluarachchi, and N. H. Jo, Use of frit-disc crucibles for routine and exploratory solution growth of single crystalline samples, Philosophical Magazine 96, 84 (2016).
- [46] T. J. Slade and P. C. Canfield, Use of refractory-volatile element deep eutectic regions to grow single crystalline intermetallic compounds, Zeitschrift für anorganische und allgemeine Chemie 648, e202200145 (2022).
- [47] R. T. Azuah, L. R. Kneller, Y. Qiu, P. L. Tregenna-Piggott, C. M. Brown, J. R. Copley, and R. M. Dimeo, Dave: a comprehensive software suite for the reduction, visualization, and analysis of low energy neutron spectroscopic data, Journal of research of the National Institute of Standards and Technology 114, 341 (2009).
- [48] J. Rodríguez-Carvajal, Recent advances in magnetic structure determination by neutron powder diffraction, Physica B: Con-

- densed Matter 192, 55 (1993).
- [49] D. Martien, M. Williamsen, S. Spagna, R. Black, T. DaPron, T. Hogan, and D. Snow, An ultrasensitive differential capacitive dilatometer, IEEE Transactions on Magnetics 55, 1 (2019).
- [50] L. Ke, R. Flint, and Y. Lee, Accurate calculation of light rareearth magnetic anisotropy with density functional theory, arXiv 2508.19496 (2025), arXiv:2508.19496 [cond-mat.mtrl-sci].
- [51] Y. Lee, Z. Ning, R. Flint, R. J. McQueeney, I. I. Mazin, and L. Ke, Importance of enforcing hund's rules in density functional theory calculations of rare earth magnetocrystalline anisotropy, npj Computational Materials 11, 168 (2025).
- [52] M. Xu, Y. Lee, X. Ke, M.-C. Kang, M. Boswell, S. L. Bud'ko, L. Zhou, L. Ke, M. Li, P. C. Canfield, and W. Xie, Giant Uniaxial Magnetocrystalline Anisotropy in SmCrGe₃, Journal of the American Chemical Society 146, 30294 (2024).
- [53] M. E. Gazzah, P.-H. Chang, Y. Lee, H. Bhandari, R. Regmi, X. Zhou, J. F. Mitchell, L. Ke, I. I. Mazin, and N. J. Ghimire, Doping-induced spin reorientation in kagome magnet tmmn6sn6 (2025), arXiv:2505.02936 [cond-mat.mtrl-sci].
- [54] P. Blaha, K. Schwarz, G. K. H. Madsen, D. Kvasnicka, J. Luitz, R. Laskowski, F. Tran, and L. D. Marks, WIEN2k: An Augmented Plane Wave plus Local Orbitals Program for Calculating Crystal Properties (Vienna University of Technology, Austria, 2018).
- [55] V. I. Anisimov, I. V. Solovyev, M. A. Korotin, M. T. Czyżyk, and G. A. Sawatzky, Density-functional theory and NiO photoemission spectra, Phys. Rev. B 48, 16929 (1993).
- [56] D. D. Koelling and B. N. Harmon, A technique for relativistic spin-polarised calculations, Journal of Physics C: Solid State Physics 10, 3107 (1977).
- [57] C. Li, A. J. Freeman, H. J. F. Jansen, and C. L. Fu, Magnetic anisotropy in low-dimensional ferromagnetic systems: Fe monolayers on Ag(001), Au(001), and Pd(001) substrates, Phys. Rev. B 42, 5433 (1990)

Supplemental Information - Hidden symmetry-breaking in a kagome Ising ferromagnet

Tianxiong Han,^{1,2} Tyler J. Slade,¹ Liqin Ke,^{1,3} Qing-Ping Ding,¹ Minseong Lee,⁴ R. D. McKenzie,^{1,2} Bing Li,^{1,5} Dhurba R. Jaishi,^{1,2} Yongbin Lee,¹ D. M. Pajerowski,⁵ Qiang Zhang,⁵ Tao Hong,⁵ P. C. Canfield,^{1,2} Y. Furukawa,^{1,2} K. Thirunavukkuarasu,⁶ Aashish Sapkota,¹ Rebecca Flint,^{1,2} and R. J. McQueeney^{1,2}

¹Ames National Laboratory, U.S. DOE, Iowa State University, Ames, Iowa 50011, USA
²Department of Physics and Astronomy, Iowa State University, Ames, Iowa 50011, USA
³Department of Materials Science and Engineering, University of Virginia, Charlottesville, VA 22904
⁴National High Magnetic Field Laboratory, Los Alamos National Laboratory, Los Alamos, New Mexico 87545, USA
⁵Oak Ridge National Laboratory, Oak Ridge, TN, 37831, USA
⁶Florida A&M University, Tallahassee, FL 32307 USA
(Dated: November 12, 2025)

X-RAY DIFFRACTION

Table S1 show results of refinements obtained with ShelxL of the single-crystal x-ray diffraction data for TbV₆Sn₆ at temperatures T=300 K, 100 K, and 80 K. Measurements were made with a Rigaku XtaLab Synergy-S diffractometer. The changes of the composition in final refinement are negligible ($\leq 0.5\%$).

POWDER NEUTRON DIFFRACTION REFINEMENT

Consistent with the previous reports of the FM ordering of the Tb moments, Fig. S1 shows the additional magnetic intensities at $\mathbf{k} = (0,0,0)$ at 1.6 K powder diffraction patterns. Additional peaks other than the one corresponding to P6/mmm crystal symmetry of TbV₆Sn₆ were identified to be from other impurity phases, such as Sn(9%) and Al_2O_3 (1%). For the magnetic Rietveld refinement, maximal magnetic symmetries corresponding to P6/mmm crystal symmetry and propagation vector $\mathbf{k} = (0, 0, 0)$ were calculated by the magnetic symmetry analysis tools using the Bilbao Crystallographic Server [S1–S4]. In our magnetic refinements, we found that magnetic symmetry P6/mm'm' best fits the data, as shown in Fig.S1 (b). Magnetic symmetry P6/mm'm' is basically a FM magnetic structure with moment along the caxis. The refined magnetic moment for Tb is 8.6(4) μ_B at T = 1.6 K.

NMR MEASUREMENTS

The nuclear magnetic resonance (NMR) measurements of $^{51}\mathrm{V}$ nuclei were conducted on a single crystal and loosely packed powder using a laboratory-built phase-coherent spinecho pulse spectrometer by sweeping the magnetic field B at fixed resonance frequencies. Fig.S2 shows the NMR spectra measured in the magnetically ordered state [S5], where the horizontal axis $\Delta \vec{B}$ is the difference between the Larmor field \vec{B}_0 and the applied field \vec{B} . For measurements above $10~\mathrm{K}$ without Tb ordering, the nuclear spin-spin relaxation rate $1/T_2$ increases rapidly. This leads to a strong reduction of the

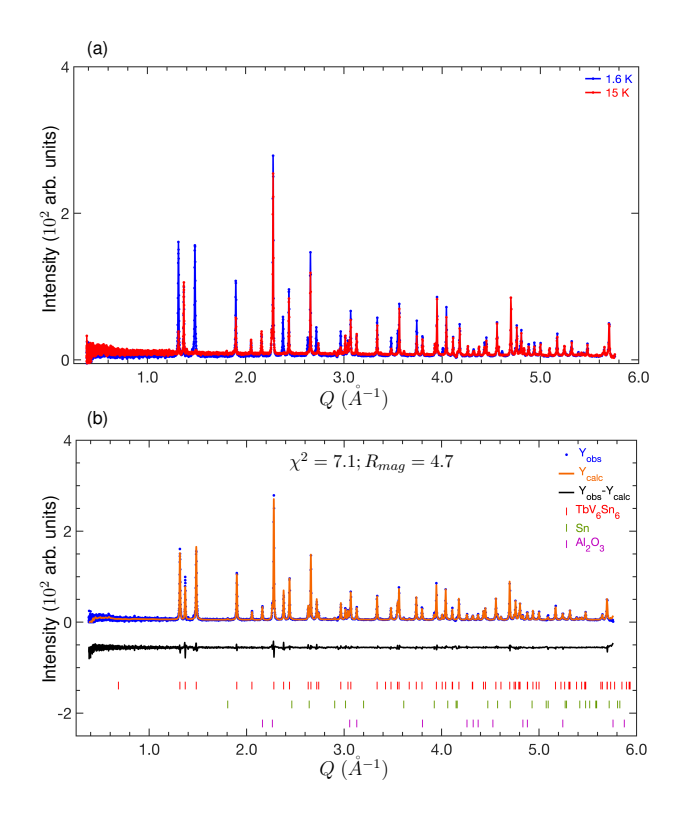


FIG. S1. (a). Time-of-flight neutron powder data for TbV $_6$ Sn $_6$ measured at 15 and 1.6K K, illustrating the appearance of additional magnetic intensities at 1.6 K. (b) Rietveld refinement of the 1.6 K powder data with magnetic symmetry P6/mm'm' and $\chi^2=6.2\%$ and $R_{mag}=3.9$. Blue dots and orange solid lines correspond to the data and calculated patterns, respectively. The black line is the difference between the data and the calculation. Additionally, red, green, and magenta vertical lines correspond to the allowed Bragg reflections for TbV $_6$ Sn $_6$ and impurities listed in the figures, respectively.

NMR signals, making the measurements difficult.

The shift of the NMR spectra ΔB is due to an internal field at the V site originating from the hyperfine field $\vec{B}_{\rm hf}$, a classical dipolar field from Tb ordered moments $\vec{B}_{\rm dip}$, and a macroscopic field $\vec{B}_{\rm macro}$. The hyperfine term includes $\vec{B}_{\rm trans}$ and $\vec{B}_{\rm 3d}$, which refer to the transferred hyperfine field between Tb ordered moments and V nuclear spins, and electronic-nuclear

TABLE S1. Refinements of single-crystal x-ray data for TbV₆Sn₆.

	TbV ₆ Sn ₆			
Temperature	295 K (RT)	100 K	80 K	
Space group	P6/mmm	P6/mmm	P6/mmm	
Lattice constant $a(Å)$	5.5244(2)	5.5138(2)	5.5133(2)	
Lattice constant $c(Å)$	9.1905(3)	9.1718(3)	9.1691(3)	
α	90	90	90	
β	90	90	90	
γ	120	120	120	
Volume (Å ³)	242.907(2)	241.483(2)	241.368(2)	
Z	1	1	1	
Collected Θ_{min}	3.360	3.367	3.367	
Collected Θ_{max}	31.936	31.715	31.723	
Reflection collected	6534	6624	6584	
Independent reflections	379	375	375	
Reflections $(I > 2\sigma(I))$	371	369	370	
Goodness-of-fit	1.242	1.162	1.116	
$R_1 [I \geq 2\sigma(I)]$	0.0122	0.0102	0.0100	
$wR_2 [I \ge 2\sigma(I)]$	0.0277	0.0235	0.0227	
R_1 [all data]	0.0126	0.0105	0.0102	
wR_2 [all data]	0.0278	0.0236	0.0228	
Largest peak/ hole	1.060/-1.771	1.975/-1.206	2.319 / -0.991	

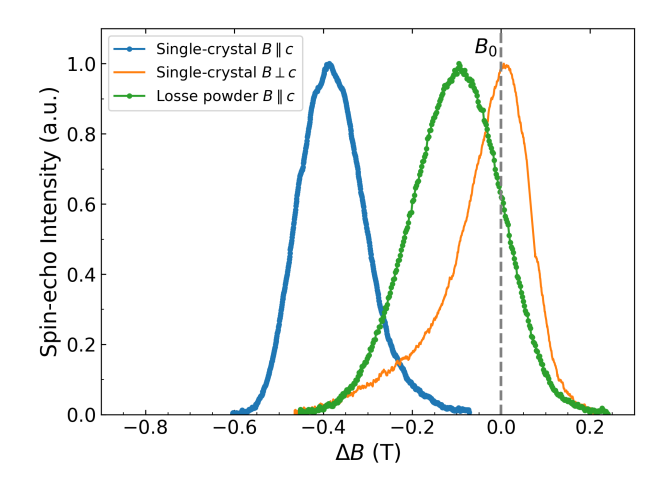


FIG. S2. NMR measurement on single crystal and powder samples at T=1.6 K. The intensity is plotted versus the differences of fields ΔB between the applied field and the Larmor field $B_0=7.0$ T.

spin coupling on the V itself, respectively. The macroscopic field \vec{B}_{macro} includes demagnetization field $\vec{B}_{\text{dem}} = -\mu_0 N \vec{M}$ and the Lorentz field $\vec{B}_{\text{L}} = \mu_0 \vec{M}/3$, where N is the demagnetization factor $N \approx 1$ for $H \parallel c, N \approx 0$ for $H \parallel ab$ in the plate-like shaped single crystal with the c-axis prependicular to the plane, and N=1/3 in powder sample. Fig. S2 shows that there is no shift for $H \perp c$, , indicating that all internal fields are parallel to c (we now drop the vector labels for B).

We observe a shift $\Delta B=-0.39(1)$ T determined from the peak position of the spectrum in the single crystal for $H\parallel c$ and $\Delta B=-0.10(1)$ T in the field-aligned powder sample. As the difference originates from the demagnetization term, we estimate $B_{\rm dem}=-0.44(1)$ T and $B_{\rm L}=0.15(1)$ T for M||c. These values are in good agreement with the calculated

TABLE S2. Local field (T) on V site from NMR measurements. The positive or negative sign represents parallel or antiparallel to the applied field B. The resonance frequency is f=78.35 MHz, corresponding to Larmor field $B_0=7.0$ T.

Sample shape	В	$B_{ m hf}$	$B_{ m dip}$	$B_{ m macro}$	
		B_{trans} B_{3d}		$B_{ m dem}$	$B_{ m L}$
Plate crystal $(N = 1)$	7.39(1)	-0.23(1)	0.13(1)	-0.44(1)	0.15(1)
Powder $(N = 1/3)$	7.10(1)	-0.23(1)	0.13(1)	-0.15(1)	0.15(1)

value in the following section. The dipolar field term $B_{\rm dip}=0.13~{\rm T}$ is calculated by a lattice sum with $9.0\mu_B/{\rm Tb}$ aligning along the c-axis. Hence, the hyperfine field is $B_{\rm hf}\approx B_{\rm trans}+B_{\rm 3d}=-0.23(1)~{\rm T}$. For clarity and ease of interpertation, all contributing local field components are listed in Table S2.

Estimating each value of B_{trans} and B_{3d} in B_{hf} is difficult from the present NMR results. Therefore, we here refer to the hyperfine coupling constant A of the V ions in the similar rareearth bearing compound YbV₆Sn₆ [S6] where A along the c axis has been reported to be a positive value of $0.0105T/\mu_B$. This indicates that the sum B_{trans} and B_{3d} are positive in YbV₆Sn₆, differing from the negative value of -0.23(1) T (or $A = -0.026(1) \text{ T}/\mu_{\text{B}}$) in TvV₆Sn₆. Since the sign of B_{trans} is expected to be the same in two compounds with the same structure, the negative sign in TbV₆Sn₆ should originate not from B_{trans} but from the negative contributions in B_{3d} . Here we attribute it to the negative core-polarization field from V-3d electrons. Using a typical value of the hyperfine coupling constant for 3d electron core-polarization (-10.5 T/ μ_B [S7]) and the observed hyperfine field of -0.23(1) T, the possible V magnetic moment are tentatively estimated to be $0.022(1)\mu_B$.

RAMAN MEASUREMENTS

Raman measurements on TbV_6Sn_6 were performed using a custom-built free beam optical setup coupled to a PPMS magnet, shown in Fig.S3. A laser with 532 nm wavelength was used for excitation, and back-scattered light in the Faraday geometry was sent to a Princeton Raman spectrometer with liquid nitrogen cooled CCD detector. The incident laser power of 3 mW was chosen to obtain reliable spectra without heating the sample. The Raman spectra was collected at selected temperatures between 300 K and 2 K. The Raman spectra at magnetic field from 0 T to 14 T were obtained at the lowest measured temperature 2 K.

Fig.S3 shows (a) temperature dependent Raman spectra in the sbsence of magnetic field and (b) Raman spectra with varying magnetic fields between 0 T and 14 T at 2 K. The vertical offset were added in the spectra for clarity. As evident from the Fig.S3, the TbV_6Sn_6 crystal does not show an obvious change in the energy of the phonon modes with decreasing temperature and increasing magnetic field. This suggests that there is an absence of any phase transitions or modifications in the local symmetry of the atoms involved.

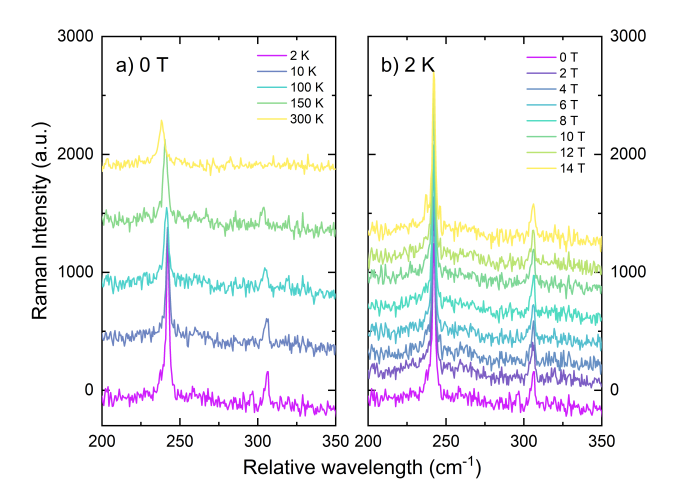


FIG. S3. Raman scattering in (a) zero-field as a function of temperature and (b) 2 K as a function of field applied along the *c*-direction (Faraday geometry).

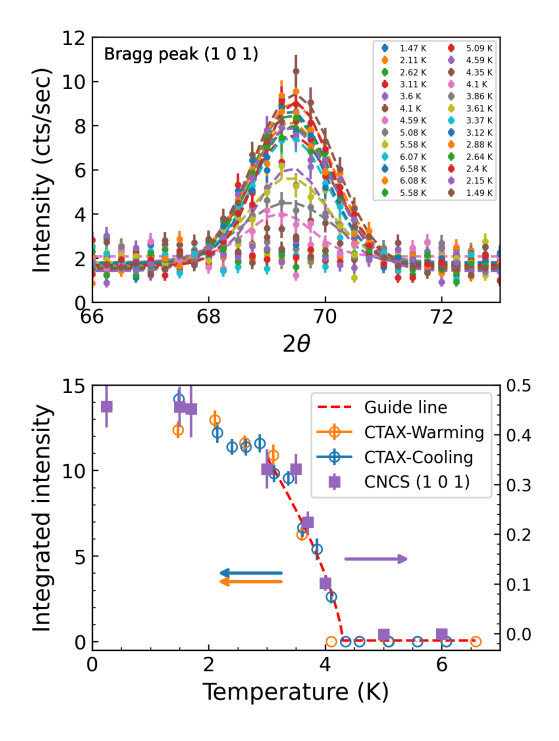


FIG. S4. (a) Data from longitudinal scans across the (1,0,1) Bragg peak at various temperatures and the fitting to Gaussian line shapes are shown as dashed lines. (b) The temperature dependence of the integrated $(1\ 0\ 1)$ Bragg peak intensities with error bars. The dashed line is a guide for the eyes using $T_C=4.3(1)$ K.

POWDER NEUTRON DIFFRACTION

Ferromagnetic order parameter

Figure S4 shows the temperature dependence of the intensity of (1,0,1) Bragg peak measured at CTAX, ORNL with $E_i\,=\,3.5$ meV. These data indicate the temperature dependence of the intensity of the second seco

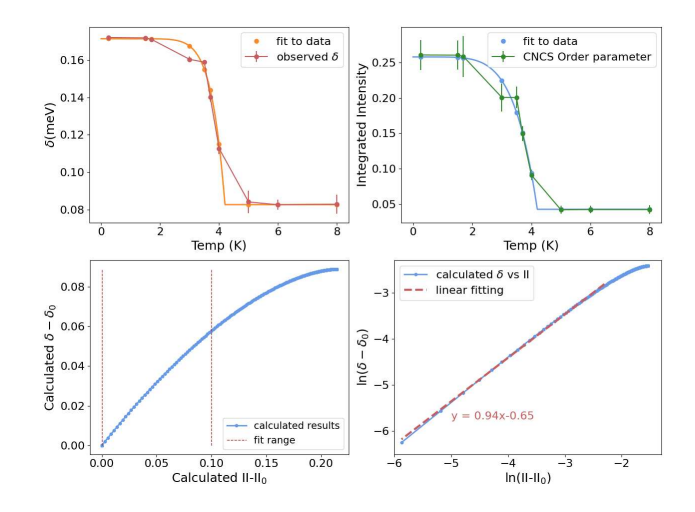


FIG. S5. (a) Averaged δ in the main text and fitted versus temperatures. (b) The temperature dependence of the integrated (1 0 0) Bragg peak intensities with error bars. (c). Calculated δ versus integrated intensities after subtracting the constants above $T_{\rm C}$. The vertical lines indicate the range picked close to $T_{\rm C}$ for fitting in the (d) panel. (d). Logarithm of the δ vs integrated intensities in the range picked, with the linear fitting with slope k=0.94.

dence of the magnetic order parameter. Fits of Gaussian line shapes to magnetic Bragg peaks showed no significant shifts in the peaks' centers nor significant changes to their FWHMs below the transition temperature. The estimated $T_C=4.4~\rm K$ is consistent with the previous reported results [S8, S9]. The integrated intensity of the peak (1~0~1) from CNCS powder measurement is plotted in Figure S4 (b) as well, showing consistent behavior with the CTAX results.

The splitting δ , as well as the integrated intensities on Bragg peak $(1\ 0\ 0)$ measured at CNCS, are plotted and fitted versus temperatures, as shown in Fig.S5. To interpret the relation between δ and magnetization $M=\sqrt{\Pi-\Pi_0}$, we fit a linear relationship with $\ln{(\delta-\delta_0)}=k\ln{(\Pi-\Pi_0)}+c$ near T_C . The fitted slope k=0.94 indicates the splitting $\delta \propto M^2$.

Short-range magnetic order

Short-range magnetic correlations above the ferromagnetic ordering temperature $T_{\rm C}=4.4~{\rm K}$ were revealed by powder inelastic neutron scattering measurements at CNCS, as shown in Figure S6(a). To isolate the quasi-elastic magnetic signal, the intensity was integrated over an energy range $\Delta\hbar\omega \leq 0.15~{\rm meV}$ and data collected at $T=60~{\rm K}$ were used as a paramagnetic background for subtraction. The resulting spectrum exhibits broad, temperature-dependent features centered at the positions corresponding to FM Bragg peaks. To interpret this behavior, we calculated the magnetic structure factor for an FM cluster containing six nearest-neighbor ${\rm Tb}^{3+}$ ions in a triangle lattice, as shown in Figure S6(b). The corre-

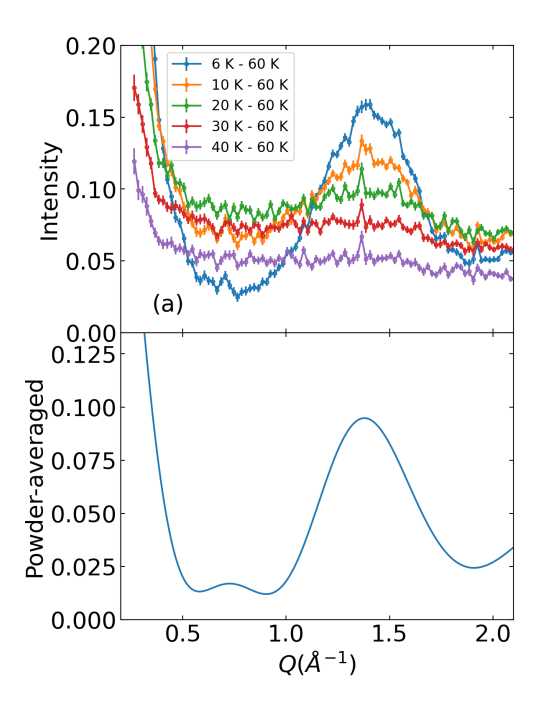


FIG. S6. (a) Short-range magnetic correlations obtained from powder inelastic neutron scattering measurements at CNCS. The data were integrated over an energy range $\Delta\hbar\omega \leq 0.15$ meV and the T=60 K dataset was subtracted. (b) Calculated powder-averaged structure factor for Tb $^{3+}$ spin cluster on triangular lattice with ion spacing $a=5.51 \mbox{\normalfont\AA}$.

lation function is written as

$$I \propto F(Q)^2 \sum_{i,j} \langle S_i S_j \rangle e^{i\mathbf{Q} \cdot (\mathbf{R}_i - \mathbf{R}_j)} (1 - \frac{Q_z^2}{Q^2})$$

where Q is the momentum transfer, F(Q) is the magnetic form factor, and \mathbf{R}_i is the atomic position. The powder-averaged intensity is calculated by averaging over all directions of \mathbf{Q} . The calculated profile captures the key features observed in the experimental data, supporting a picture of short-range FM correlations persisting above $T_{\mathbf{C}}$.

SINGLE-CRYSTAL INELASTIC NEUTRON SCATTERING

Transverse mode dispersion

The main CEF transition from $|6\rangle \rightarrow |5\rangle$ is a strong transverse excitation that can be used to estimate key magnetic interactions. For a simple triangular ferromagnet with nearest-neighbor intralayer (\mathcal{J}) and interlayer coupling (\mathcal{J}_z), the dispersion in terms of the total angular momentum J can be written as

$$\hbar\omega = 2JD + 2J\mathcal{J}_z(1 - \cos 2\pi L) + 2J\mathcal{J}[3 - \cos 2\pi (H - K) - \cos 2\pi (H + K) - \cos 4\pi K]$$
(S1)

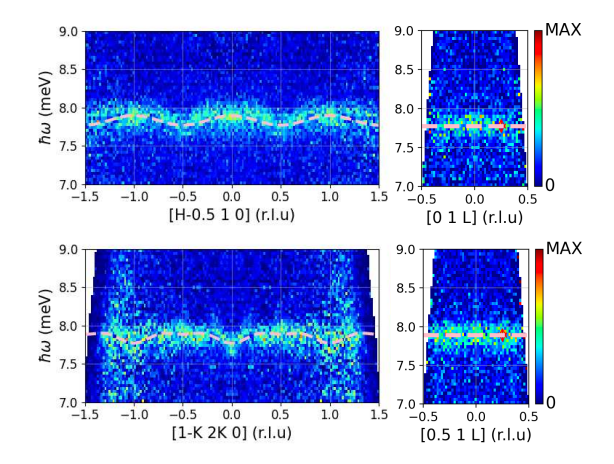


FIG. S7. Spin wave dispersion along [H-0.5 1 0], [1-K 2K 0], [0 1 L]and [0.5 1 L] directions. The pink dashed line is the fitted dispersion relation from linear spin wave theory and the red arrow indicates the instrument resolution.

where (H,0,0) and (-K,2K,0) are orthogonal vectors in the hexagonal plane. D is the single-ion anisotropy that can be obtained from the CEF parameters according to the relation $D=-K_1/J^2$ where $K_1=-3J^{(2)}B_2^0-40J^{(4)}B_4^0-168J^{(6)}B_6^0$ is the magnetic anisotropy constant. Our CEF parameters estimated at 0.25 K $(B_2^0=-0.112,\,B_4^0=-5.41\text{E-}4,\,B_6^0=2.31\text{E-}6,\,$ and $B_6^6=2.30\text{E-}6$ meV) find a uniaxial anisotropy parameter D=-0.641 meV.

We fit the energy spectra from single-crystal INS measurements shown in Fig. S7 to Eq. S1, with fitted interaction and anisotropy interaction being $\mathcal{J}=-2.4(2)~\mu\text{eV}$, D=-0.65(1)~meV, and $|\mathcal{J}_z|<0.0015~\text{meV}$. The calculated dispersion from linear spin-wave theory is plotted in the pink dashed line over the dispersion data.

Estimation of dipolar interactions

The dipole-dipole interactions between Tb moments are given by

$$\mathcal{H}_{dip} = \frac{\mathcal{P}}{2} \sum_{i \neq j} \sum_{\mu\nu} \mathcal{L}_{ij}^{\mu\nu} J_i^{\mu} J_j^{\nu}, \tag{S2}$$

where

$$\mathcal{L}_{ij}^{\mu\nu} = \frac{1}{r_{ij}^3} \left(\delta_{\mu\nu} - \frac{3r_{ij}^{\mu} r_{ij}^{\nu}}{r_{ij}^2} \right) \tag{S3}$$

and $\mathcal{P} = \mu_0 (g_J \mu_B)^2/(4\pi)$. Considering the strong uniaxial anisotropy of Tb ions, we estimate the contribution of the dipolar interactions to the local field on a Tb site for long-range order with wavevector **k** and moments aligned perpendicular to the triangular layer. In a mean-field approximation, the dipolar energy is

$$E_0(\mathbf{k}) = \frac{1}{2} \mathcal{P} J_z^2 L^{zz}(\mathbf{k})$$
 (S4)

TABLE S3. Dipolar sums for TbV_6Sn_6 with moments aligned perpendicular to the triangular layer (in meV). A local field correction appropriate for a long needle-shaped domain is made in the FM case $(\mathbf{k} = 0)$.

k	$E_0(\mathbf{k})$ (meV)	B_{local}^{z} (T)
(0,0,0)	+0.0666	-0.112
(1/2,1/2,0)	-0.0268	0.103
(0,0,1/2)	+0.1410	-0.541

where $L^{zz}(\mathbf{k}) = \sum_j \mathcal{L}_{0j}^{zz} \cos(\mathbf{k} \cdot \mathbf{r}_{0j})$. This energy can also be represented as a local magnetic field B_0^z acting on the Tb moment $m_z = g_J \mu_{\rm B} J_z$.

$$B_0^z = -\mathcal{P}J_z L^{zz}(\mathbf{k})/(g_J \mu_{\rm B}) = -\frac{2E_0(\mathbf{k})}{m_z}$$
 (S5)

For FM order, this local field must also be corrected for demagnetization effects given by

$$B_{local}^z = B_{Lorentz} - \mu_0 NM + B_0^z \tag{S6}$$

where N is the demagnetization factor and $B_{Lorentz}=\mu_0 M/3$ is the net field inside a spherical cavity of a uniformly magnetized volume. For TbV $_6$ Sn $_6$, $M=\frac{9\mu_{\rm B}}{\sqrt{3}a^2c/2}$ from which we obtain $B_{Lorentz}=0.1438$ T. For a needle-shaped FM domain with N=0, the local field is $B_{local}^z=B_{Lorentz}+B_0^z$.

Table S3 shows select dipolar energies and local fields for the simple hexagonal Tb sublattice with c/a=1.66. Stripetype AFM order [$\mathbf{k}=(1/2,1/2,0)$] is favored over FM order [$\mathbf{k}=(0,0,0)$] within the triangular layer. This clearly establishes that dipolar coupling competes with a dominant RKKY-type FM exchange within the layer. From calculations of the dipolar coupling using Eqn. S3, we estimate that $\mathcal{J}_{dip}^{zz}/\mathcal{J}_{RKKY}\approx -0.2$ for nearest-neighbors within the layer.

The dispersionless character of excitations along (0,0,L) shown in Fig. S7 indicate very small interlayer magnetic interactions and establish the quasi-2D character of TbV₆Sn₆. The interlayer interactions leading to long-range FM order could be dipolar in character and we estimate a FM dipolar coupling of $\mathcal{J}_z' \approx -.00031$ meV for interlayer nearest-neighbors. However, the long period magnetic incommensurability along L, as reported for GdV₆Sn₆ [S10], may also indicate a role for weak intralayer RKKY interactions.

- [S1] M. I. Aroyo, J. M. Perez-Mato, C. Capillas, E. Kroumova, S. Ivantchev, G. Madariaga, A. Kirov, and H. Wondratschek, Bilbao crystallographic server: I. databases and crystallographic computing programs, Zeitschrift für Kristallographie-Crystalline Materials 221, 15 (2006).
- [S2] M. I. Aroyo, A. Kirov, C. Capillas, J. Perez-Mato, and H. Wondratschek, Bilbao crystallographic server. ii. representations of crystallographic point groups and space groups, Foundations of Crystallography 62, 115 (2006).
- [S3] M. I. Aroyo, J. M. Perez-Mato, C. Capillas, and H. Won-dratschek, The bilbao crystallographic server, International Tables for Crystallography 1, 57 (2006).

- [S4] J. Perez-Mato, S. Gallego, E. Tasci, L. Elcoro, G. de la Flor, and M. Aroyo, Symmetry-based computational tools for magnetic crystallography, Annual Review of Materials Research 45, 217 (2015).
- [S5] The subtle feature of the spectrum can be roughly reproduced with a nuclear quadrupole frequency of $\nu_{\rm q}=0.37$ MHz, and an asymmetry parameter of electric field gradient of $\eta=0.86$.
- [S6] S. Park, H. Sakai, S. Hosoi, S. M. Thomas, S. Kambe, Y. Tokunaga, A. P. Dioguardi, J. D. Thompson, F. Ronning, M. Kimata, T. Furukawa, T. Sasaki, E. D. Bauer, and M. Hirata, Investigation of the paramagnetic state of the kagome kondo lattice compound YbV₆Sn₆: a ⁵¹V nuclear magnetic resonance study (2025), arXiv:2506.04563 [cond-mat.str-el].
- [S7] A. J. Freeman and R. E. Watson, Magnetism, in *Magnetism*, Vol. IIA, edited by G. T. Rado and H. Suhl (Academic Press, New York, 1965) Chap. 4, pp. 167–305.
- [S8] G. Pokharel, B. Ortiz, J. Chamorro, P. Sarte, L. Kautzsch, G. Wu, J. Ruff, and S. D. Wilson, Highly anisotropic magnetism in the vanadium-based kagome metal ${\rm TbV_6Sn_6}$, Phys. Rev. Mater. **6**, 104202 (2022).
- [S9] E. Rosenberg, J. M. DeStefano, Y. Guo, J. S. Oh, M. Hashimoto, D. Lu, R. J. Birgeneau, Y. Lee, L. Ke, M. Yi, and J.-H. Chu, Uniaxial ferromagnetism in the kagome metal TbV₆Sn₆, Phys. Rev. B **106**, 115139 (2022).
- [S10] Z. Porter, G. Pokharel, J.-W. Kim, P. J. Ryan, and S. D. Wilson, Incommensurate magnetic order in the F₂ kagome metal GdV₆Sn₆, Phys. Rev. B 108, 035134 (2023)